

# The kinematics of the large western knot in the halo of the young planetary nebula NGC 6543

Deborah L. Mitchell<sup>1</sup>,<sup>\*</sup> M. Bryce<sup>1</sup>, J. Meaburn<sup>2</sup>, J.A. López<sup>2</sup>,  
M. P. Redman<sup>3</sup>, D. Harman<sup>3</sup>, M. G. Richer<sup>2</sup> and H. Riesgo<sup>2</sup>

<sup>1</sup>*Jodrell Bank Observatory, University of Manchester, Macclesfield SK11 9DL, UK*

<sup>2</sup>*Instituto de Astronomía, Universidad Nacional Autónoma de México, Apartado Postal 877, 22800 Ensenada, B.C., México*

<sup>3</sup>*Department of Physics, National University of Ireland Galway, College Rd., Galway, Ireland.*

<sup>4</sup>*Astrophysics Research Institute, Liverpool John Moores University, Twelve Quays House, Egerton Wharf, CH41 1LD, UK*

Accepted ... Received...

## ABSTRACT

A detailed analysis is presented of the dominant ionised knot in the halo of the planetary nebula NGC 6543. Observations were made at high spectral and spatial resolution of the [O III]  $\lambda 5007$  Å line using the Manchester echelle spectrometer combined with the 2.1-m San Pedro Martir Telescope. A 20-element multislit was stepped across the field to give almost complete spatial coverage of the large western knot and surrounding halo.

The spectra reveal, for the first time, gas flows around the kinematically inert knot. The gas flows are found to have velocities comparable to the sound speed as gas is photo-evaporated off an ionised surface. No evidence is found of fast wind interaction with the knot and we find it likely that the fast wind is still contained in a pressure-driven bubble in the core of the nebula. This rules out the possibility of the knot having its origin in instabilities at the interface of the fast and AGB winds. We suggest that the knot is embedded in the slowly expanding Red Giant wind and that its surfaces are being continually photoionised by the central star.

**Key words:** circumstellar matter – stars: mass-loss – stars: winds, outflows – stars: kinematics – ISM: planetary nebulae: individual: NGC 6543.

## 1 INTRODUCTION

NGC 6543 (RA 17<sup>h</sup> 58<sup>m</sup> 33<sup>s</sup>.4 & Dec+66° 37' 59".0 [J2000.0]) is one of the brightest and most structurally complex planetary nebulae (PNe) known. The central star is an 07+WR type, which has a high-speed (1900 kms<sup>-1</sup>) particle wind (Patriarchi & Perinotto 1991). The bright core of the nebula appears as two concentric crossed ellipses in projection with their major axes orientated at position angles 25° and 115° respectively (Miranda & Solf 1992). Balick et al. (1987) detected two bright polar caps aligned with the major axis of the 25° ellipse and two twisted jet-like features extending radially outwards from the caps. Balick, Wilson, & Hajian (2001) discovered a series of nine regularly spaced concentric rings around the core of NGC 6543 in archival HST images. The best estimate of distance to NGC 6543 is 1001 ± 269 pc (Reed et al. 1999), which was measured directly from the expansion parallax.

The bright core of NGC 6543 is surrounded by a faint, extended, spherical halo (Millikan 1974) of radius 165 arcsec

(Middlemass, Clegg, & Walsh 1989). Chu, Jacoby, & Arendt (1987) defined NGC 6543 as having a Type I detached halo. The halo has a very filamentary appearance and contains a large, bright, irregularly-shaped knot located 100 arcsec west of the core. The halo of NGC 6543 is unusually bright in [O III]  $\lambda 5007$  Å (Middlemass et al. 1989) despite the fact that the main PN shell also shows bright [N II]  $\lambda 6584$  Å emission, suggesting a complex overall structure. Bryce et al. (1992) found the halo to be kinematically inert with a maximum expansion velocity of 4.5 kms<sup>-1</sup>, despite its explosive, filamentary appearance. They found that both the bright knot and halo are centred on the systemic heliocentric radial velocity of  $V_{\text{sys}} = -68.5$  kms<sup>-1</sup>, confirming that the knot and halo are physically linked. An [O III]  $\lambda 5007$  Å and [N II]  $\lambda 6584$  Å composite image that features both the halo and core of NGC 6543 is shown in Fig. 1 with the dominant ionised knot being considered here.

The bright knot in the halo of NGC 6543 is highly unusual in that it is relatively large and is a unique feature within the halo. Middlemass, Clegg, & Walsh (1989) calculated that the knot has an electron temperature of  $T_e = 14700$  K using [O III] $\lambda\lambda 4959 + 5007/4363$  line intensity

<sup>\*</sup> E-mail: dlm@jb.man.ac.uk (DLM)

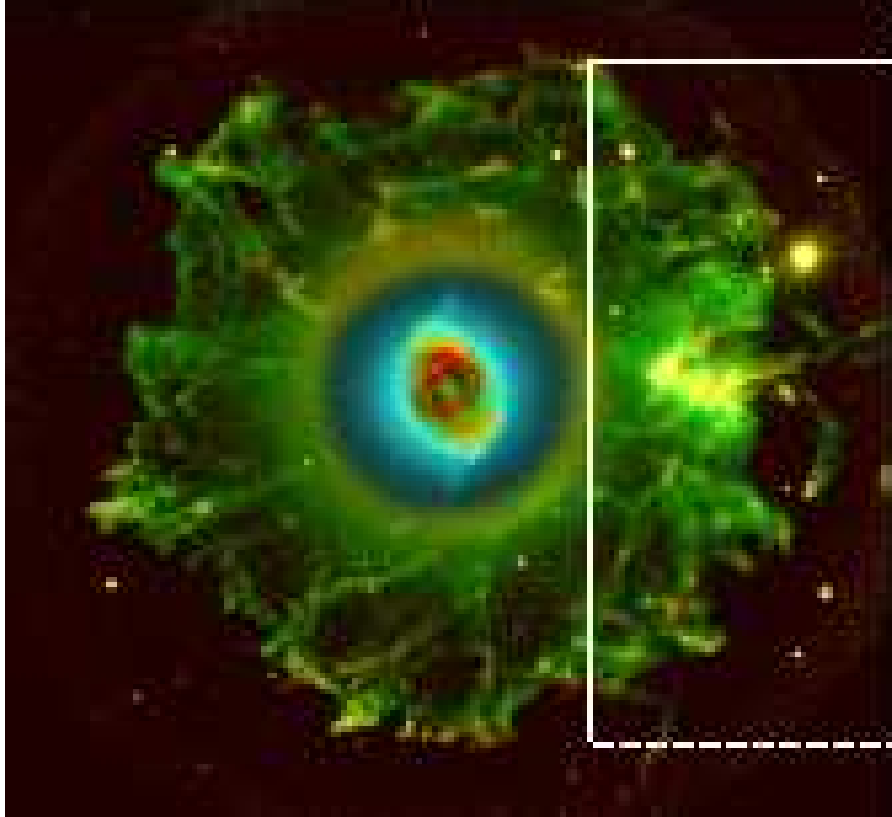


**Figure 1.** A composite image showing the core and halo of NGC 6543 taken with the Nordic Optical Telescope.  $[\text{N II}] \lambda 6584 \text{ \AA}$  is shown in red and  $[\text{O III}] \lambda 5007 \text{ \AA}$  in blue and green. The image is  $385'$  by  $352'$  in extent. North is to the top and east is to the left. The dashed box outlines the region covered by the multislit (see section 2). The image shows the complex nebula core, which consists of two crossed ellipses in projection, and jets protruding from the polar caps of the shell. Also visible is the large, filamentary halo surrounding the core and the prominent knot in the west. Credit R. Corradi (Isaac Newton Group) and D. Goncalves (Inst. Astrofisica de Canaries).

ratios. Meaburn et al. (1991) derived a much lower  $T_e$  of  $8860 \pm 1000$  K from observations of the thermal broadening of the  $\text{H}\alpha$  and  $[\text{N II}] \lambda 6584 \text{ \AA}$  lines. In order to account for this discrepancy, a mass-loaded wind model was proposed, which predicts that a supersonic stellar wind percolates through the clumpy core and mass-loads in the process. The mass-loaded wind then percolates into the halo, which adds heat and raises the temperature of the  $[\text{O III}] \lambda 5007 \text{ \AA}$  region (but see section 4.1 for an alternative explanation).

At present, very little is known about the origin of the knot and what physical processes have affected its morphology since its formation. The low global expansion velocity of the halo, the low turbulence in the bright knot gas and the evidence that an ionisation front is present on the knot surface (the  $[\text{N II}] \lambda 6584 \text{ \AA}$  ridge is displaced from the parallel  $[\text{O III}] \lambda 5007 \text{ \AA}$  one) all suggest that the large knot is the dense relic of the Red Giant wind, now being photoionised on its surface. The observations to be reported here aim to determine whether or not this knot, and hence the whole halo, is subject to the fast wind from the central star; if so, high-speed flows of ablated gas would be expected in the faint regions in the close vicinity of this knot. For this purpose,  $[\text{O III}] \lambda 5007 \text{ \AA}$  line profiles have been obtained with a stepped multi-slit, giving unprecedented spatial coverage, over the whole vicinity of the unusual knot.

## 2 OBSERVATIONS AND DATA REDUCTION

The Manchester echelle spectrometer (Meaburn et al. 2003) combined with the 2.1-m, f/8 San Pedro Martir (MES-SPM) telescope was used in its secondary mode to take direct images at  $[\text{O III}] \lambda 5007 \text{ \AA}$  and  $[\text{N II}] \lambda 6584 \text{ \AA}$  of the bright knot located in the western part of the halo of NGC 6543. The images, shown in Figs. 2 and 3, were taken during an observing run on the SPM telescope in Mexico in June 2004, using a SITe3 CCD with  $1024 \times 1024$   $24 \mu\text{m}$  square pixels ( $\equiv 0.31'' \text{ pixel}^{-1}$ ). Integration times were 1800s for both images.

Spatially resolved, longslit observations of the bright knot were taken using the MES in its primary spectral mode during the same observing run. The observations were taken through a narrow-band (30 Å) filter, which isolates the  $[\text{O III}] \lambda 5007 \text{ \AA}$  emission line in the 114th echelle order.

A 20-element multislit was used to cover the knot with parallel north-south slit positions. Each slit is separated by 10.75 arcsec ( $\equiv 69 \text{ km s}^{-1}$ ), each slit being  $70 \mu\text{m}$  wide ( $\equiv 0.9''$  and  $5 \text{ km s}^{-1}$ ). Three integrations of 1800 secs were obtained, between each of which, the multislit was offset to the west by approximately 3 arcsec. The net result is almost total spatial coverage of the knot by 60 parallel north-south slits, as shown in Fig. 4.  $2 \times 2$  binning was adopted during the observations, giving 512 pixels in the spectral (x) direction ( $\equiv 4.79 \text{ km s}^{-1} \text{ pixel}^{-1}$ ) and 512 pixels in the spatial (y) direction ( $\equiv 0.62'' \text{ pixel}^{-1}$ ). Each slit is 317 arcsec long and

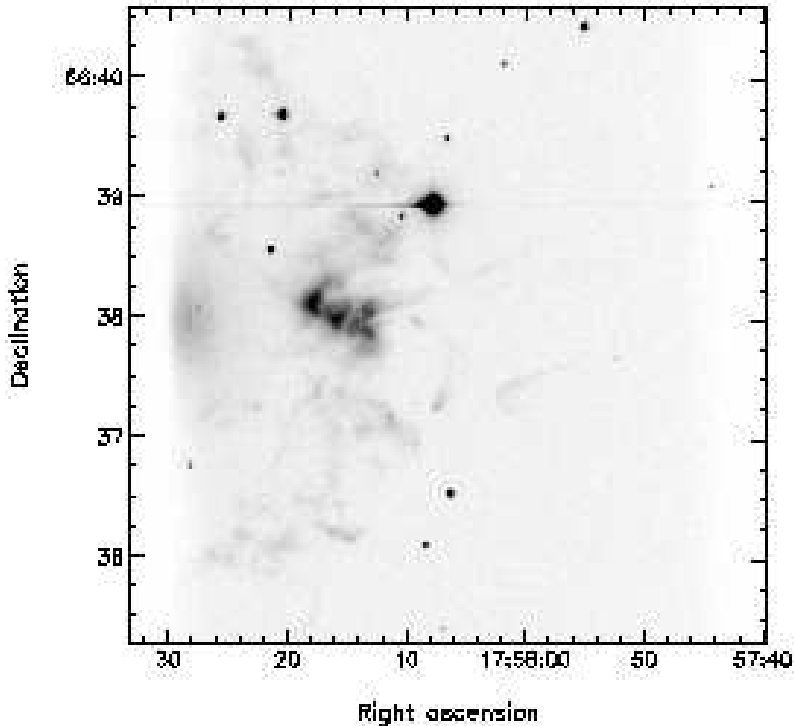


**Figure 2.** A narrowband [O III]  $\lambda 5007 \text{ \AA}$  image of the western part of the halo of NGC 6543, showing the bright knot around RA  $17^{\text{h}} 58^{\text{m}} 16^{\text{s}} 0$  & Dec  $+66^{\circ} 37' 59''$  [J2000.0]. The central star of the PN is located  $100''$  east of the knot. The star at RA  $17^{\text{h}} 58^{\text{m}} 08^{\text{s}} 0$  & Dec  $+66^{\circ} 38' 55''$  is overexposed, which has resulted in horizontal bleeding across the CCD.

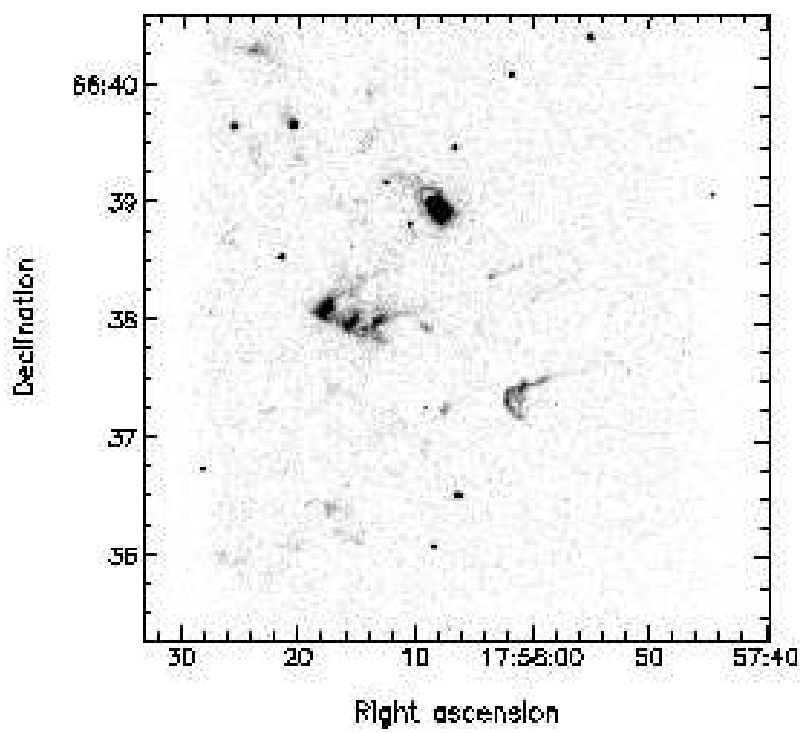


**Figure 3.** A narrowband [N II]  $\lambda 6584 \text{ \AA}$  image of the region shown in Fig. 2 (the bright star is contaminated by a filter ghost).

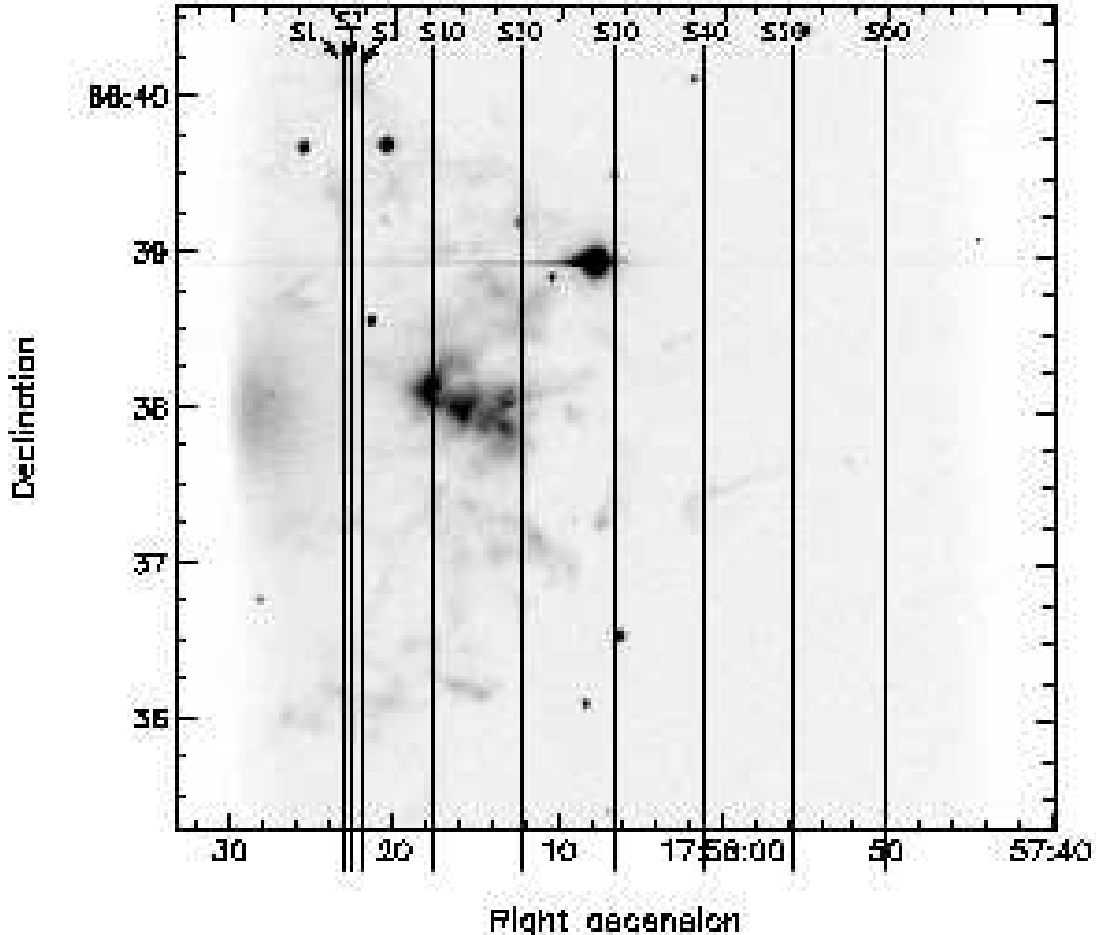


**Figure 4.** [O III]  $\lambda 5007 \text{ \AA}$  image of the knot region (Fig. 2) with a sample of the 60 slit positions superimposed (S1, S2, S3, S10, S20, S30, S40, S50 and S60). Each slit position is separated by  $\sim 3''$ . The full extents of the slit lengths on the sky are illustrated here.

a total distance of 213 arcsec in the E-W direction is covered by the dataset (slit 1 to slit 60).

Data reduction was performed using STARLINK software. The [O III]  $\lambda 5007 \text{ \AA}$  spectra were bias-corrected and cleaned of cosmic rays. The spectra were then wavelength calibrated against a ThAr emission line lamp. A ThAr spectrum from a single slit was used to aid the line identification process in the multislit spectrum due to the complication of overlapping arc lines from adjacent slits.

The three calibrated multislit [O III]  $\lambda 5007 \text{ \AA}$  position-velocity (pv) arrays were sliced up in a direction parallel to the slit lengths to give 60 pv arrays, each containing emission from a single slit. The 60 pv arrays were then stacked in sequence from east to west using the program FORMCUBE (Malcolm Currie, private communication) to produce a pv data cube where the E-W spatial direction has been reconstructed. The data cube has spatial dimensions of  $317'' \times 213''$  (in the N-S and E-W directions, respectively) and a dispersion dimension ranging from heliocentric radial velocities  $V_{\text{hel}} = -34$  to  $-103 \text{ kms}^{-1}$  with a velocity resolution of  $7 \text{ kms}^{-1}$ .

### 3 RESULTS

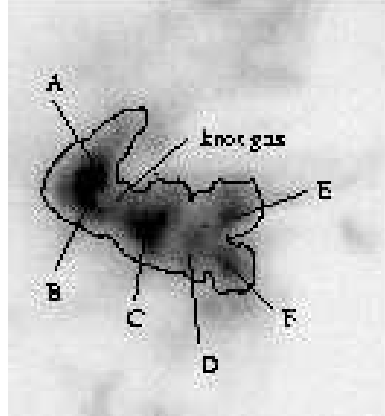
#### 3.1 Direct images

Fig. 5 shows a subset of the [O III]  $\lambda 5007 \text{ \AA}$  image (Fig. 2) in order to reveal the substructure in the bright knot (Meaburn et al. 1991). It is clear that the knot is composed of several smaller sub-knots, which have been labelled A-F in Fig. 5 (following Bryce 1992). The sub-knots are embedded in a relatively bright region of gas identified in Fig. 5, as ‘knot gas’. The outline of the knot gas is marked on the image.

#### 3.2 Combined image

The datacube was collapsed along the dispersion axis to produce an image showing the whole range in  $V_{\text{hel}}$ . This effectively represents a narrowband [O III]  $\lambda 5007 \text{ \AA}$  image of the knot.

Fig. 6 shows this combined image at low contrast in order to highlight structure in the faint halo that surrounds the knot. The dark, horizontal bands at cross-sections 185, 420 and 490 are continuum emission from field stars. The image reveals that the bright knot gas is surrounded by much



**Figure 5.** An extracted region of the [O III]  $\lambda 5007 \text{ \AA}$  image that shows the knot and the faint halo immediately surrounding it. The image is shown at high-contrast to reveal substructure in the knot. The brightest features (sub-knots) have been labelled A-F. The sub-knots are embedded in bright ‘knot-gas’ and the boundary between the knot gas and the faint, background halo is outlined on the image.

fainter ‘halo gas’ and the boundary between the two regions is distinct. The faint halo gas is present both to the north and south of the knot region. The southern emission (cross-sections 120 to 280) has a more filamentary appearance than the faint halo gas in the north. A faint plume of gas is located north of the knot, between cross-sections 360 and 400, labelled G, which is orientated in a north-west direction. Trails of gas appear to emanate from the northern edge of the knot, labelled H and I, which have similar orientations to plume G. Two distinct features lie south-west of the knot, labelled J and K, both of which have a comet-like appearance (these features are also clear in Figs. 2 and 3).

### 3.3 Velocity Slices

The datacube was sliced up along the dispersion axis to create radial velocity slices, each of width  $10 \text{ kms}^{-1}$ . The velocity planes within each slice were co-added to create two-dimensional images. The images reveal how the morphology of the knot varies with  $V_{\text{hel}}$ . Emission was detected in three of the images,  $I_1$ ,  $I_2$  and  $I_3$ , which are shown at high and low contrast in Figs. 7 and 8, respectively. The high-contrast images have been normalised with respect to the maximum intensity. Co-ordinates of features within the images are expressed as (NS, EW) pixels and arcsecs, respectively. The NS axis is expressed in pixels for ease of comparison between Figs. 7, 8, 9 and 10. The velocity ranges covered by each image are listed in Table 1. Note that  $I_2$  is centred on  $V_{\text{sys}}$ . The images show the following features and trends:

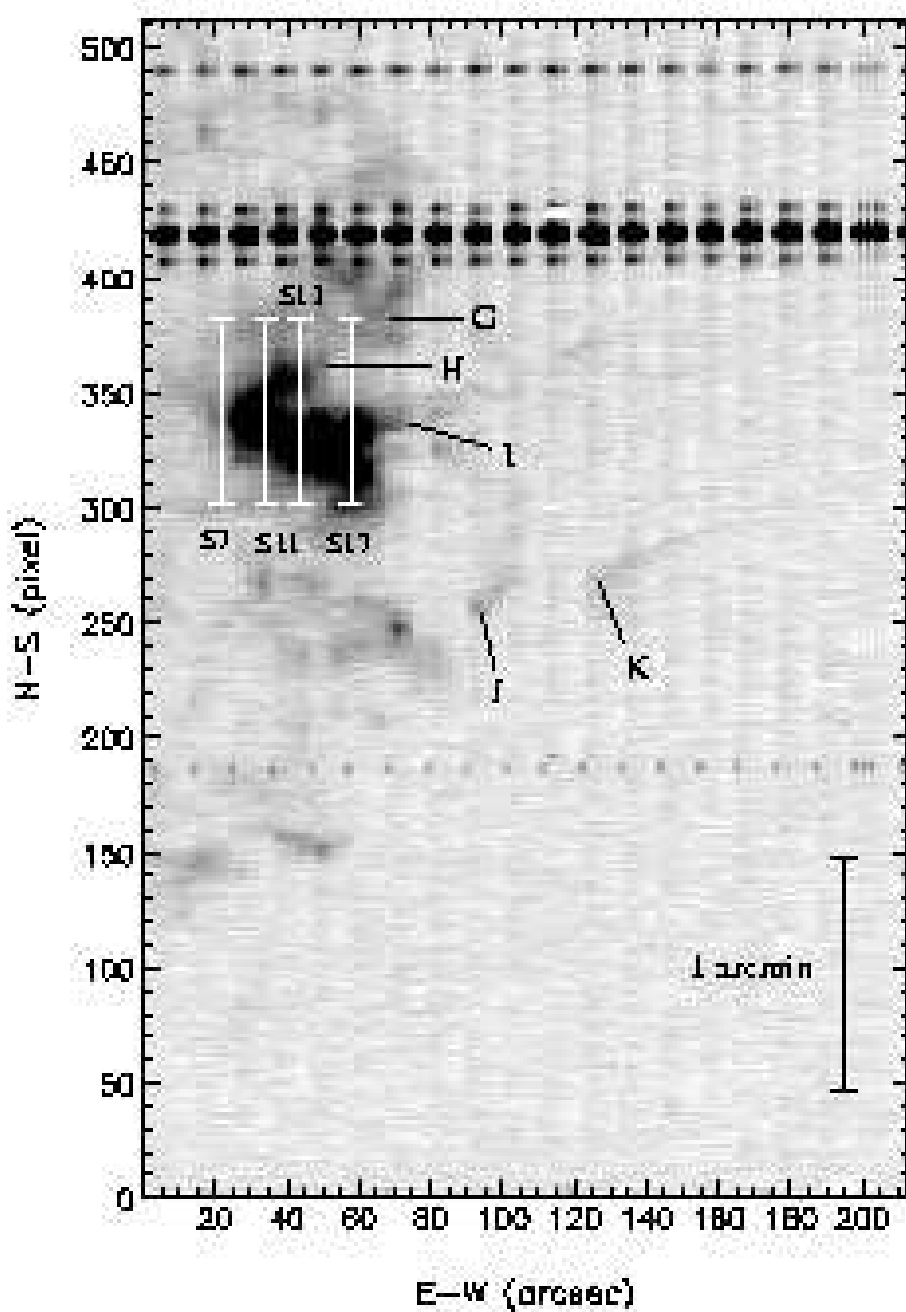


**Figure 6.** The total velocity range of the [O III]  $\lambda 5007 \text{ \AA}$  datacube is shown at low-contrast in order to highlight faint structure in the halo. The N-S extent of the figure is shown in Fig. 1. The slit length of 512 pixels  $\equiv 317 \text{ arcsec}$ . The plume of gas located to the north of the knot has been labelled G; two trails of gas are labelled H and I; the comet-like features in the south-west are labelled J and K. The lines labelled S7, S11, S13 and S17 mark the lengths of slits from which the corresponding  $V_{\text{hel}}$  and line width plots are shown in Figs. 9 and 10, respectively. The striped horizontal bands at cross-sections 185, 420 and 490 are continuum features from field stars (if a star hits one slit it appears in this image as though it is in all 20 slits).

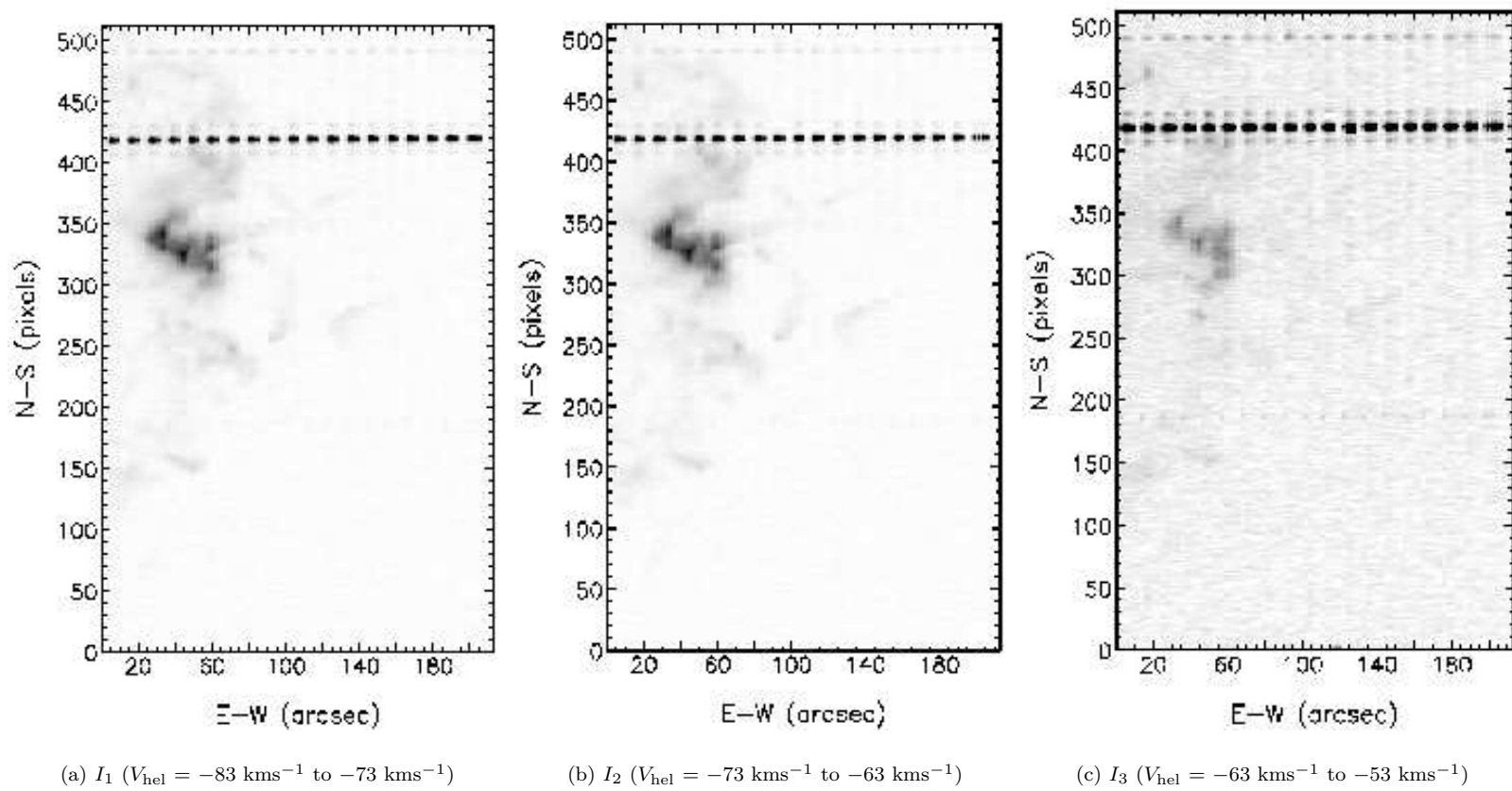


**Figure 7.** The knot shown at different velocity intervals,  $I_1$ ,  $I_2$  and  $I_3$ , (see Table 1). The images are shown at high-contrast in order to highlight substructure within the knot.

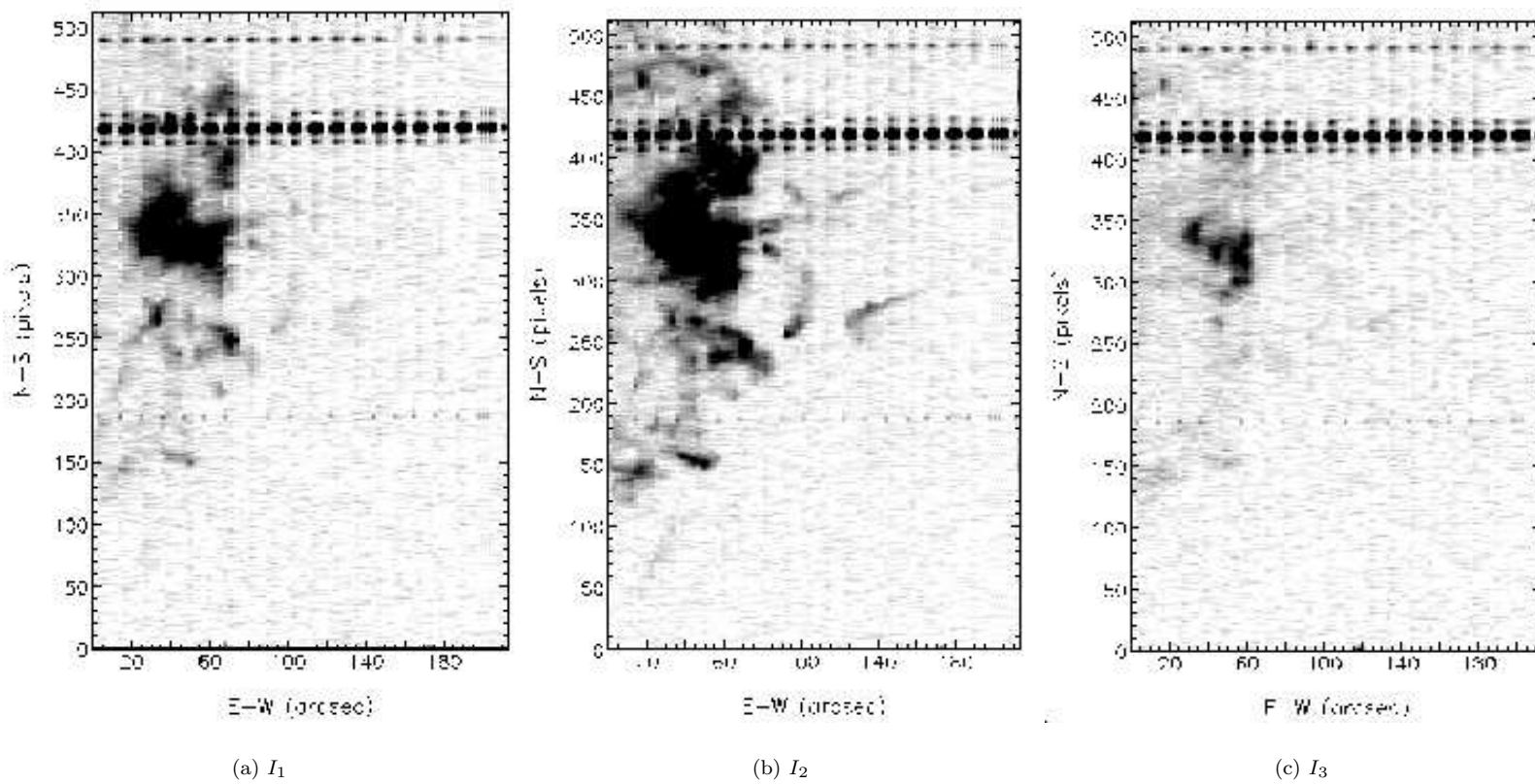


**Figure 8.** As Fig. 7, but shown at low-contrast in order to reveal faint substructure in the halo that surrounds the knot.

Image	$V_{min}/\text{kms}^{-1}$	$V_{max}/\text{kms}^{-1}$
$I_1$	-83	-73
$I_2$	-73	-63
$I_3$	-63	-53

**Table 1.** Ranges in  $V_{\text{hel}}$  of the collapsed datacube slices that contain [O III]  $\lambda 5007 \text{ \AA}$  emission.

(i) Most of the [O III]  $\lambda 5007 \text{ \AA}$  emission from the filamentary halo surrounding the knot is present in  $I_2$  (Fig. 8b). Halo material located to the south of the knot is also visible in  $I_1$  (Fig. 8a), whereby the filaments situated at pixel 270, 30 arcsecs and pixel 250, 70 arcsecs are particularly bright in this image. In contrast, the halo has virtually no red-shifted component of  $V_{\text{hel}}$ :  $I_3$  (Fig. 8c) reveals very little diffuse emission, except for a compact feature at pixel 270, 50 arcsecs. The gas in the halo, therefore, has a very narrow velocity range.

(ii) The knot gas has a large blue-shifted component of  $V_{\text{hel}}$  as similar levels of emission are present in  $I_1$  and  $I_2$ . The knot gas surrounding the eastern half of the knot is particularly bright in  $I_1$ . The knot gas is completely absent in  $I_3$ . It appears that the knot gas has a more extensive velocity range than the faint halo gas.

(iii) Features A - K (Figs. 5 and 6) are all bright in  $I_2$  (Fig. 8b). Trails H and I are both present in  $I_1$ , whereby trail H is particularly bright around pixel 360, 40 arcsecs (Fig 7a). The comet-like features, F and G, are also faintly present in  $I_1$ , as is the western half of plume G. All of these features are completely absent, however, in  $I_3$ .

(iv) Sub-knots A, B and C are much brighter than sub-knots E and F in  $I_1$ . This suggests that the western side of the knot has a higher recessional component of  $V_{\text{hel}}$  than the eastern side.

### 3.4 Line profiles

The manual fitting program LONGSLIT was used to fit single Gaussian profiles to the [O III]  $\lambda 5007 \text{ \AA}$  line profiles from each slit. The profiles were first binned together into blocks of two along the slit length that covered the bright knot and blocks of either three or four along the slit length that covered the surrounding, faint halo gas, in order to improve the signal-to-noise ratio in each profile. The program was used to produce plots of  $V_{\text{hel}}$  and the full width half maxima (FWHM) of the fitted profiles as a function of the slit length. The line profiles are calibrated to  $\pm 1 \text{ kms}^{-1}$  in absolute heliocentric velocity. The trends in  $V_{\text{hel}}$  from sections of four of the slits that cover the knot,  $S_7$ ,  $S_{11}$ ,  $S_{13}$  and  $S_{17}$ , are shown in Figs. 9a - 9d (the positions of the slits are marked on Fig. 6). These slit positions were selected as they exhibit velocity trends that are representative of those found at different spatial positions across the knot. The corresponding trends in FWHM of the fitted Gaussians are shown in Figs. 10a - 10d. The unit of cross-section along the y-axis in these figures corresponds to increments in pixels along the slit length. Note that as  $V_{\text{sys}} = -68.5 \pm 1.0 \text{ kms}^{-1}$ , any  $V_{\text{hel}}$  greater than this value will be considered red-shifted and any  $V_{\text{hel}}$  less than this value will be considered blue-shifted. The velocity trends observed over each slit are summarised below:

(i)  $S_7$ : The gas bordering the eastern edge of the knot shows a trend of becoming increasingly red-shifted in a northwards direction (Fig 9a). The plot of line width against slit length (Fig. 10a) reveals a region of very inert gas at cross-section 340, which corresponds to the position of the eastern apex of the knot (Fig. 6).

(ii)  $S_{11}$ : Sub-knots A and B have very similar values of  $V_{\text{hel}}$ , which lie close to  $V_{\text{sys}}$  of the knot (Fig. 9b). The knot gas immediately north of sub-knot A (cross-sections 346 - 362) shows increasingly blue-shifted velocities in a northwards direction. A reversal in velocity trend is observed at cross-section 365, whereby the Gaussian profile centres become increasingly red-shifted in a northwards direction. This reversal in velocity trend corresponds to the transition from the knot gas to the fainter gas identified as plume G in Fig. 6. The blue-shifted profiles observed in the knot gas region are broader than the profiles from the sub-knots and are generally broader than the red-shifted profiles observed in the region of the faint halo gas (Fig. 10b). The narrowest line profiles are associated with the faint halo gas to the south of the knot (cross-section 318).

(iii)  $S_{13}$ : The plot of  $V_{\text{hel}}$  against slit length for  $S_{13}$  (Fig. 9c) shows very similar trends to that of  $S_{11}$  (Fig. 9b). The emission from sub-knot C (cross-sections 320 - 330) lies at  $V_{\text{sys}}$  of the knot. A trend towards blue-shifted velocities is observed in the knot gas region north of the knot between cross-sections 340 - 380. The observed line profiles from this blue-shifted knot gas are relatively broad (Fig. 10c) with an observed width of approximately  $12 \text{ kms}^{-1}$ . The faint halo gas located to the far north (cross-sections 380 - 400) of the field is red-shifted relative to  $V_{\text{sys}}$  of the knot. The line profiles from this faint halo gas are narrower than those from the knot gas.

(iv)  $S_{17}$ : Sub-knots E and F correspond to the blue-shifted ‘dips’ (cross-sections 330 and 315, respectively) in Fig. 9d. The sub-knots have narrower line profiles than the surrounding knot gas (Fig. 10d). The emission located south of sub-knot F (cross-sections 300 - 310) shows exceptional behaviour in that it is red-shifted relative to the sub-knots. Although this gas appears to be very close to the sub-knots and therefore we might expect it to constitute part of the knot gas, Fig. 5 shows that this red-shifted region of gas lies just outside of the knot-gas boundary. This suggests it may be a line-of-sight effect of a background filament in the halo.

## 4 DISCUSSION

The plots in Fig. 10 show that all of the observed [O III]  $\lambda 5007 \text{ \AA}$  profiles from the knot are very narrow (observed profile widths generally less than  $12.5 \text{ kms}^{-1}$ ). This supports the findings of Bryce et al. (1992), who concluded that both this prominent knot and the whole halo are kinematically inert.

The width of an observed [O III]  $\lambda 5007 \text{ \AA}$  emission line profile is the result of the combination of several broadening mechanisms. In this case, the important broadening mechanisms are thermal broadening, instrumental broadening and turbulent broadening. The observed line profile can be modelled as a Gaussian profile of width  $\Delta V_{\text{obs}}$ , which is the convolution of the profiles corresponding to each of the indi-

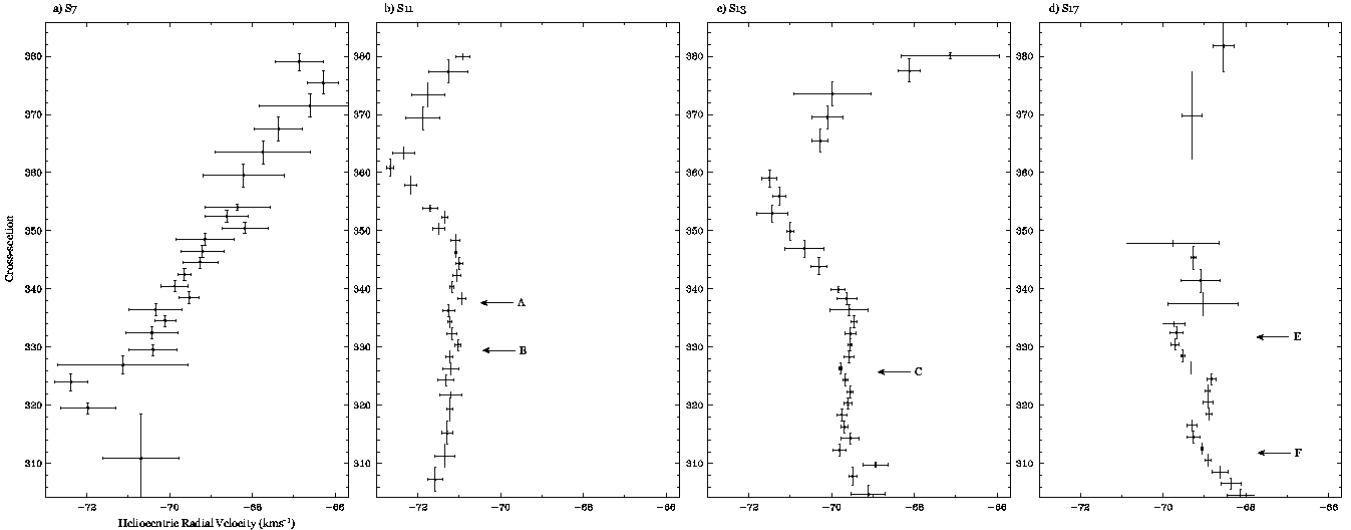


**Figure 9.** Centroids of best-fit Gaussians to observed [O III]  $\lambda 5007 \text{ \AA}$  profiles ( $\equiv V_{\text{hel}}$ ) from slit sections marked on Fig. 6. The positions of sub-knots A, B, C, E and F are labelled on the plots.

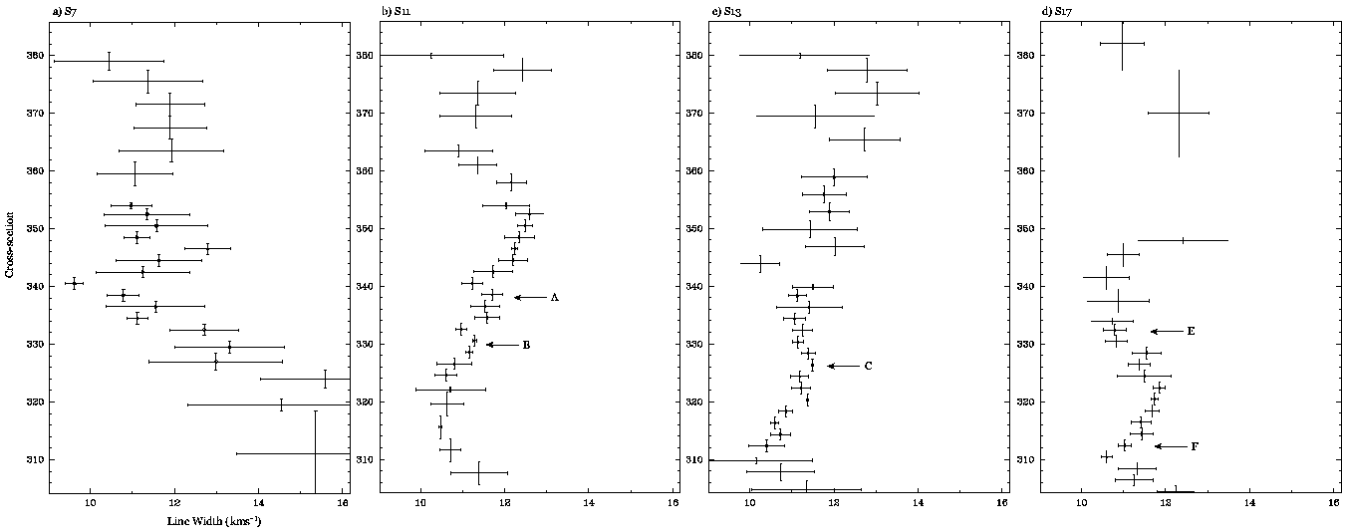


**Figure 10.** Full width half maxima of best-fit Gaussians to observed [O III]  $\lambda 5007 \text{ \AA}$  profiles (see Fig. 9).

vidual broadening processes. If each individual component is also modelled as a Gaussian then

$$\Delta V_{\text{obs}}^2 = \Delta V_{\text{th}}^2 + \Delta V_{\text{inst}}^2 + \Delta V_{\text{turb}}^2 \quad (1)$$

where  $\Delta V_{\text{th}}$ ,  $\Delta V_{\text{inst}}$  and  $\Delta V_{\text{turb}}$  are the values of the thermal broadening, instrumental broadening and turbulent broadening, respectively.

If the gas is in thermal equilibrium, then the thermal broadening is due to the Maxwellian distribution of the Doppler shifts of the emitted photons. This component has a full width at half maximum (FWHM) of

$$\Delta V_{\text{th}} = 2 \sqrt{\frac{2kT_e \log_e 2}{m}} \quad (2)$$

where  $k$  is Boltzmann's constant,  $T_e$  is the [O III]  $\lambda 5007 \text{ \AA}$  electron temperature and  $m$  is the atomic mass of oxygen.

The  $T_e$  of 8860 K derived by Meaburn et al. (1991) will be adopted (see Section 4.1) and this gives a  $\Delta V_{\text{th}}$  of  $5 \text{ km s}^{-1}$ . The instrumental broadening can be determined from the FWHM of the Gaussians fitted to the arc line profiles, which in this case is approximately  $7 \text{ km s}^{-1}$ .

Sub-knots A to F all show similar velocity characteristics: each sub-knot has a  $\Delta V_{\text{obs}}$  of approximately  $11.5 \text{ km s}^{-1}$ . Using Equation 1, this gives a typical  $\Delta V_{\text{turb}}$  across the knot of  $7.6 \text{ km s}^{-1}$ . The sub-knots all exhibit a  $V_{\text{hel}}$  close to  $V_{\text{sys}}$ . The sub-knots are, therefore, very stable, kinematically inert objects.

The knot gas, however, exhibits complex motions over short spatial scales. Figs. 10a to 10d show that the line profiles of the knot gas (cross-sections 350 to 360 and 300 to 310) are generally broader than the line profiles of the sub-knots, with a  $\Delta V_{\text{turb}}$  of approximately  $9.0 \text{ km s}^{-1}$  [note that these profiles are only broad relative to the profiles of the

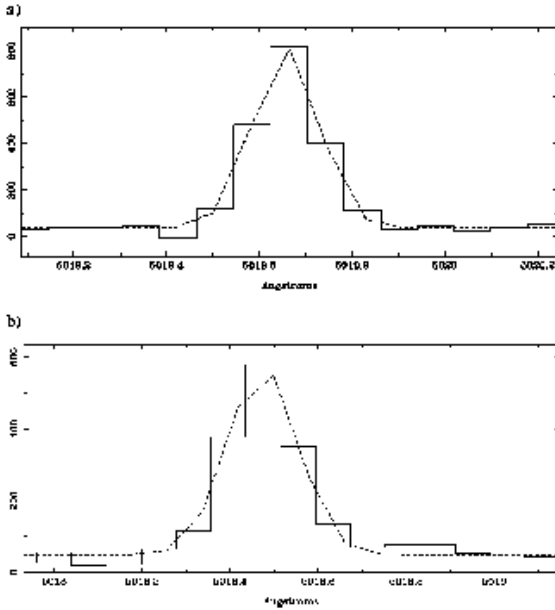


**Figure 11.** Sample profiles showing single Gaussian fits to (a) a narrow profile from the knot gas at the eastern apex of the knot (S7 cross-sections 339 - 340), (b) a broad profile from the halo gas to the north of the knot (S11 cross-sections 379 - 381).

sub-knots and are still much narrower than the typical line widths observed from the bright core of NGC 6543 [Meaburn et al. 1991)]. Both the velocity slices (Figs. 7 and 8) and the plots of  $V_{\text{hel}}$  (Fig. 9) show that knot gas has a larger blue-shifted component of  $V_{\text{hel}}$  than both the sub-knots and the halo gas. This is most likely an optical depth effect in the dense knot; only the expansion from the near-side of the globule is seen and the far-side emission is absorbed.

In contrast, the observed line widths of the knot gas surrounding the eastern apex of the knot (cross-section 340) are very narrow (Fig. 10a). Using Equation 1 it is found that the gas in this region has a  $\Delta V_{\text{turb}}$  of just  $4.7 \text{ km s}^{-1}$ . The sample profiles shown in Fig. 11 demonstrate that it is appropriate to fit both the narrow and broad profiles with single Gaussians albeit with different widths.

The bright knot gas and the surrounding faint halo differ in their velocity characteristics. The line profiles in the faint halo gas are generally narrower than in the knot gas. In addition, there is a trend towards increasingly red-shifted velocities moving northwards from the boundary between the two regions (Figs. 9a - c).

The relatively turbulent nature of the knot gas surrounding the sub-knots provides evidence of a gas flow around the knot. The very narrow line profiles in the east are most likely to coincide with the apex of the flow. The relatively broad, blue-shifted profiles associated with trail H (Fig. 9b cross-section 360) indicate that the trail is most likely to be material that has been ablated from the knot rather than a filament in the background halo.

The gas kinematics reported here are most likely to be the result of photo-ionisation of the surface a pre-existing dense clump followed by localised expansion of the ionised gas. The ionised gas is overpressured with respect to the surroundings and expands outwards from those portions of the clump facing the star. The portions of the clump not

exposed to the direct ionizing flux of the star are in shadow but will experience a weaker diffuse radiation field that is typically  $\sim 15\%$  of the local direct field (Canto et al. 1998). The shadow region behind a neutral clump is cooler and underpressured compared to the surrounding ionized gas and is thus compressed. If this higher density gas is ionised by the diffuse flux then it can appear as a tail behind the clump (Canto et al 1998). Such a mechanism seems plausible for generating the tail structures seen around the knot and sub-knots in NGC 6543. The radiation pressure is too feeble at these distances to cause any effect on the knot while, as argued below, the wind from the star does not reach to the distance of the knots.

The adiabatic sound speed of the gas,  $c_i$ , as it evaporates off the surface of the knot is given by

$$c_i = \sqrt{\frac{\gamma k T_e}{\mu m_H}} \quad (3)$$

where  $\gamma$  is the specific heat ratio of a monatomic gas ( $= 5/3$ ),  $T_e$  is the electron temperature of the gas,  $\mu$  is the mean atomic weight of ionised hydrogen ( $= 0.5$ ) and  $m_H$  is the mass of a hydrogen atom ( $= 1.7 \times 10^{-27} \text{ kg}$ ). Assuming that the ionised gas is at the temperature derived by Meaburn et al. (1991) of  $8800 \text{ K}$ , equation 3 gives  $C_i = 16.5 \text{ km s}^{-1}$ .

The flows observed in the vicinity of the sub-knots exhibit  $\Delta V_{\text{turb}}$  less than  $15 \text{ km s}^{-1}$ . This is consistent with the sound speed expected as gas flows down the pressure gradient as it evaporates off an ionised globule surface.

#### 4.1 Knot formation and evolution

Inhomogeneities are ubiquitous in PNe (e.g. O'Dell et al. 2002) ranging from compact cometary knots (e.g. the Helix and Eskimo PNe) to large-scale, lower density clumps in the extended halos such as those being considered here.

In general, Vishniac (1994) predicted that the post-shocked gas at the interface of the fast and slow winds in a PN will become hydrodynamically unstable and non-linear instabilities will develop. Dyson et al. (1989) argued that the compact cometary knots in the Helix nebula represent surviving condensations from the atmosphere of the progenitor Red Giant star, which are ejected with the halo during the slow wind phase. There is now evidence for clumpy shell structure in AGB stars in advanced evolutionary stages: K'-band imaging of the AGB star IRC+10216 by Weigelt et al. (1998) revealed its dusty shell is highly fragmented. They predict that the knots are formed by fragmentation of the circumstellar shell due to large-scale surface convection cells. Capriotti (1973) suggested that the knots in the halo of NGC 6543 (Fig. 1) are formed far from the central star as a result of Rayleigh-Taylor instabilities forming where the ionisation front expands into the neutral Red Giant wind ejecta.

Steffen & López (2004) describe the two possible mechanisms responsible for the subsequent shaping of clumps and filaments after they have formed within PNe: (1) photoevaporation by ionising radiation from the central star; (2) interaction with a fast stellar wind. There are thus two possibilities for the formation and subsequent evolution for the knot in NGC 6543, both of which will be assessed based on previous evidence and the new results presented in this

paper. Since the flow velocities reported here are clearly sub-sonic with no evidence of any supersonic motions generated by a fast wind, photoevaporation (Case 1) must dominate the structure and dynamics. Previously Bryce et al. (1992) measured the global expansion of the whole halo as  $\leq 10$   $\text{km s}^{-1}$ , which is consistent with the expected expansion of a Red Giant wind (Corradi et al. 2003). Clearly we are considering an earlier stage in the mass loss history of the central star than the post-AGB phase and the onset of the fast wind.

Until recently, the presence of the fast stellar wind in the halo was considered necessary in order to account for the discrepancy between the  $T_e$  derived by Middlemass, Clegg, & Walsh (1989) and Meaburn et al. (1991), which was originally explained using the mass-loaded wind model (see section 1). However, an alternative explanation was proposed by Viegas & Clegg (1994). They were able to show that if clumps with a density greater than  $10^6 \text{ cm}^{-3}$  are present in a PN, then the [O III]  $\lambda 5007 \text{ \AA}$  nebular line is collisionally de-excited instead of undergoing a forbidden transition, and hence the average [O III]  $\lambda\lambda 4959 + 5007/4363$  line ratio would be higher and the derived  $T_e$  overestimated. Clumps in PNe have been found to have central densities of  $\sim 10^6 \text{ cm}^{-3}$  (Meaburn et al. 1992, Borkowski et al. 1993, Dopita et al. 1994, Bautista, Pradhan & Osterbrock 1994). It is reasonable to assume, therefore, that the knot in NGC 6543 has a density of the same order of magnitude.

In summary, it appears that the fast wind, or even a mass-loaded flow driven by the fast wind, is not impinging on this halo knot in NGC 6543. The fast wind remains contained in the central pressure driven bubble in the bright AGB superwind that forms the nebular core. The inner shock front will stop the fast wind having any effect on the outer halo at the present time. This conclusion rules out the possibility of the knottiness of the halo being due to instabilities between the fast wind and the earlier ejected Red Giant wind since the former has not yet reached the latter. Furthermore, knots formed via Rayleigh-Taylor instabilities are predicted to have radially symmetric structures (O'Dell et al. 2002), which is not observed in this case.

#### 4.2 Knot ionization

The ionizing flux of the central star,  $S_*$ , can be estimated from the  $H\beta$  flux of  $2 \times 10^{-10} \text{ erg cm}^{-2} \text{ s}^{-1}$  measured by Bianchi et al. (1986) using the method described in Osterbrock (1989). This gives  $S_* = 2 \times 10^{45} \text{ s}^{-1}$ . Using the distance of 1Kpc (Reed et al. 1999) gives that that knot lies at  $2.5 \times 10^{18} \text{ cm}$  from the star and so the flux incident on the knot at this distance is  $F_* = S_*/4\pi R^2 = 3 \times 10^8 \text{ s}^{-1} \text{ cm}^{-2}$ .

The ionization balance in a photoevaporating knot is given approximately by (López-Martín et al 2001; Henney 2001)

$$F_* = un_i + \alpha n_i^2 h \quad (4)$$

where  $u$  is the expansion of newly ionized material away from the ionization front,  $n_i$  is the density of the ionized gas and  $h \sim 0.1r_{\text{clump}}$  is the thickness of the ionized layer around the knot. The first term on the right hand side of equation 4 is due to the ionization of fresh neutral material while the second term is due to reionizing recombined

material. For a given local ionizing flux, there is a critical density in the ionized gas that determines which process dominates the absorption of ionizing photons. This is important because, as López-Martín et al. (2001) point out, if recombinations dominate then the surface brightness of an ionized knot matches the incident ionizing flux. If recombinations are insignificant, then the emission from the clump is much reduced and the clump will appear fainter than expected from photon balance. Henney (2001) shows that most photoevaporated flows (proplyds, Eagle pillars, Rosette globules) are recombination dominated unless the ionizing flux is small or if the distance of the clump from the source is large (Gum globules, Helix knots).

The above arguments suggest a very straightforward explanation for the puzzling brightness difference between the bright knot and other halo structures in NGC 6543 (see Fig 1). The knot is the densest part of the halo and widespread recombinations lead to a large surface brightness; essentially all of the incident ionizing photons are absorbed and re-emitted. Meanwhile, the lower density of the other features in the halo mean that they are already fully ionized or recombinations are insignificant. Using the flux value above,  $F_* = 3 \times 10^8 \text{ s}^{-1} \text{ cm}^{-2}$  and an ionized layer of  $1.5 \times 10^{16} \text{ cm}$  then from Figure 1 of Henney (2001), we require that the ionized gas around the knot have a density  $>> 3 \times 10^2 \text{ cm}^{-3}$  while the other halo features must be less dense than this. It would be interesting to use the [S II] doublet to measure the local electron density in the knot and the other halo features.

## 5 CONCLUSIONS

The results presented in this paper reveal for the first time the existence of a low-turbulence, low-velocity gas flow around the most prominent knot in the halo of NGC 6543. The flow velocities observed are comparable to the sound speed as gas flows down the pressure gradient as it photoevaporates off an ionised globule surface. Although it is known that the fast stellar wind has played an important role in shaping the complex core of the Cat's Eye nebula (Balick & Preston 1987), we find it unlikely that it has percolated into the halo, as the observed flow velocities are too low to be the result of an interaction of the fast stellar wind with the knot. We conclude that the fast wind must still be contained in a central pressure-driven bubble. Consequently, the knot cannot have been formed via an instability as the fast wind interacts with the slower Red Giant wind, and it is thus likely that the knot is a relic of the Red Giant wind. We suggest that the knot is brighter than other halo structures because it is the only feature dense enough for the ionizing photon flux to be balanced by recombinations behind the knot ionization front.

The kinematical analysis of the knot in NGC 6543 should aid understanding of how these structures form and evolve in general. A natural follow-up to these observations would be a detailed analysis of the chemical abundances of the knot and the dynamical evolution of the sub-knots (A - F) at high spatial resolution.

## ACKNOWLEDGMENTS

DLM thanks PPARC for her research studentship. We would like to thank the staff at the San Pedro Martir observatory who helped with the observations. Thanks also to Malcolm Currie at Starlink who wrote the program FORMCUBE and Romano Corradi for allowing us to use his composite image of the halo of NGC 6543 (Fig. 1).

## REFERENCES

Balick, B., Wilson, J., & Hajian, A. R. 2001, *Astronomical Journal*, 121, 354

Balick, B. & Preston, H. L. 1987, *Astronomical Journal*, 94, 958

Balick, B., Owen, R., Bignell, C. R., & Hjellming, R. M. 1987, *Astronomical Journal*, 94, 948

Balick, B. 1987, *Astronomical Journal*, 94, 671

Bautista, M. A., Pradhan, A. K., & Osterbrock, D. E. 1994, *The Analysis of Emission Lines*, 1

Bianchi, L., Cerrato, S., & Grewing, M. 1986, *Astronomy and Astrophysics*, 169, 227

Borkowski, K. J., Harrington, J. P., Tsvetanov, Z., & Clegg, R. E. S. 1993, *The Astrophysical Journal Letters*, 415, L47

Bryce, M., Meaburn, J., Walsh, J. R., & Clegg, R. E. S. 1992, *Monthly Notices of the Royal Astronomical Society*, 254, 477

Canto, J., Raga, A., Steffen, W., & Shapiro, P. 1998, *Astrophysical Journal*, 502, 695

Capriotti, E. R. 1973, *Astrophysical Journal*, 179, 495

Chu, Y., Jacoby, G. H., & Arendt, R. 1987, *The Astrophysical Journal Supplement Series*, 64, 529

Corradi, R. L. M., Sánchez-Blázquez, P., Mellema, G., Giannamico, C., & Schwarz, H. E. 2004, *Astronomy and Astrophysics*, 417, 637

Corradi, R. L. M., Schönberner, D., Steffen, M., & Perinotto, M. 2003, *Monthly Notices of the Royal Astronomical Society*, 340, 417

Dopita, M. A., et al. 1994, *Astrophysical Journal*, 426, 150

Dyson, J. E., Hartquist, T. W., & Biro, S. 1993, *Monthly Notices of the Royal Astronomical Society*, 261, 430

Dyson, J. E., Hartquist, T. W., Pettini, M., & Smith, L. J. 1989, *Monthly Notices of the Royal Astronomical Society*, 241, 625

García-Segura, G., López, J. A., & Franco, J. 2001, *Astrophysical Journal*, 560, 928

Henney, W. J. 2001, *Revista Mexicana de Astronomia y Astrofisica Conference Series*, 10, 57

Huggins, P. J. & Mauron, N. 2002, *Astronomy and Astrophysics*, 393, 273

López-Martín, L., Raga, A. C., Mellema, G., Henney, W. J., & Cantó, J. 2001, *Astrophysical Journal*, 548, 288

López, J. A., Vazquez, R., & Rodriguez, L. F. 1995, *The Astrophysical Journal Letters*, 455, L63

Meaburn, J., Clayton, C. A., Bryce, M., Walsh, J. R., Holloway, A. J., & Steffen, W. 1998, *Monthly Notices of the Royal Astronomical Society*, 294, 201

Meaburn, J., Walsh, J. R., Clegg, R. E. S., Walton, N. A., Taylor, D., & Berry, D. S. 1992, *Monthly Notices of the Royal Astronomical Society*, 255, 177

Meaburn, J., Nicholson, R., Bryce, M., Dyson, J. E., & Walsh, J. R. 1991, *Monthly Notices of the Royal Astronomical Society*, 252, 535

Mellema, G., Raga, A. C., Canto, J., Lundqvist, P., Balick, B., Steffen, W., & Noriega-Crespo, A. 1998, *Astronomy and Astrophysics*, 331, 335

Middlemass, D., Clegg, R. E. S., & Walsh, J. R. 1989, *Monthly Notices of the Royal Astronomical Society*, 239, 1

Miranda, L. F. & Solf, J. 1992, *Astronomy and Astrophysics*, 260, 397

O'Dell, C. R., Balick, B., Hajian, A. R., Henney, W. J., & Burkert, A. 2002, *Astronomical Journal*, 123, 3329

Osterbrock, D.E. 1989, *Astrophysics of Gaseous Nebulae and Active Galactic Nuclei* (Mill Valley: Univ. Science Books)

Patriarchi, P. & Perinotto, M. 1991, *Astronomy and Astrophysics*, 91, 325

Reed, D. S., Balick, B., Hajian, A. R., Klayton, T. L., Giovanardi, S., Casertano, S., Panagia, N., & Terzian, Y. 1999, *Astronomical Journal*, 118, 2430

Simis, Y. J. W., Icke, V., & Dominik, C. 2001, *Astronomy and Astrophysics*, 371, 205

Steffen, W. & López, J. A. 2004, *Astrophysical Journal*, 612, 319

Viegas, S. M. & Clegg, R. E. S. 1994, *Monthly Notices of the Royal Astronomical Society*, 271, 993

Vishniac, E. T. 1994, *Astrophysical Journal*, 428, 186

Weigelt, G., Balega, Y., Bloecker, T., Fleischer, A. J., Osterbart, R., & Winters, J. M. 1998, *Astronomy and Astrophysics*, 333, L51